RESEARCH

Electrospun polymeric nanohybrids with outstanding pollutants adsorption and electroactivity for water treatment and sensing devices

Roberto Scaffaro[1] · Andrea Maio[1] · Michele Gammino[1]

Abstract

Graphene oxide (GO) and carbon nanotubes (CNTs) were loaded at different mutual ratios into poly(vinylidene fluoride-co-hexafluoropropylene) (PVDF-co-HFP) matrix and electrospun to construct mats that were assessed as smart sorbents for decontaminating water from methylene blue (MB) pollutant, while ensuring the additional possibility of detecting the dye amounts. The results revealed that sorption capacity enhances upon increasing GO content, which is beneficial to wettability and active area. Equilibrium adsorption of these materials is precisely predicted by the Langmuir isotherm model and the maximum capacities herein achieved, ranging from 120 to 555 mg/g depending on the formulation, are higher than those reported for similar systems. The evolution of the structure and properties of such materials as a function of dye adsorption was studied. The results reveal that MB molecules prompted the increase of electrical conductivity of the samples in a dose-dependent manner. Mats containing solely CNTs, while displaying the worst sorption performance, showed the highest electrical performances, displaying interesting changes in their electrical response as a function of the dye amount adsorbed, with a linear response and high sensitivity ($309.4\ \mu S\ cm^{-1}\ mg^{-1}$) in the range 0–235 μg of dye adsorbed. Beyond the possibility to monitor the presence of small amounts of MB in contaminated water and the saturation state of sorbents, this feature could even be exploited to transform waste sorbents into high-added value products, including flexible sensors for detecting low values of pressure, human motion, and so on.

Keywords Graphene oxide · Carbon nanotubes (CNTs) · PVDF-HFP · Methylene blue removal · Methylene blue sensing · Pressure sensing

1 Introduction

The development of hybrid nanocomposites with well-defined structure and tailored properties is gaining a rising concern in the perspective to design materials with emerging properties exceeding the sum of those of starting components [1]. For instance, integrating specific additives into a polymer matrix could be advantageous to fabricate low-cost, lightweight materials that combine the versatility and processability of polymers with additional functionalities, useful for a wealth of industrial applications ranging from structural to electronic devices [2–5]. Recently, the demand for multifunctional membranes exploitable for water treatment processes is growing because of the inexorable rise of environmental pollution [6–10]. Among the several pollutants, synthetic dyes are gaining a worldwide concern since more than one million tons of 100,000 new dye products are generated annually, and at least 10–15% of them are discharged into water bodies without opportune treatments [11–15].

Among the most popular dyes, methylene blue (MB) is a cationic organic molecule that is widespread in the dyeing fabrics in clothing and textile industries and is also applied for dyeing papers and leathers [16]. Unfortunately, it is often detected in natural water in which it is highly stable and exerts various health risks for humans, as well as damaging ecosystems [1, 16, 17]. So far, several techniques have been used to remove dyes from wastewater, relying on the recovery or degradation of these target molecules. With a view to a circular economy and zero waste, the first approach should be preferable, especially if the devices adopted for the decontamination of wastewater are also reusable and easily recoverable. Among the separation techniques, batch adsorption/sequestration has a huge potential in eco-remediation

✉ Roberto Scaffaro
 roberto.scaffaro@unipa.it

[1] Department of Engineering, University of Palermo, Viale Delle Scienze, Ed. 6, 90128 Palermo, Italy

of dye-containing wastewater due to its cost-effectiveness and simplicity when compared to other strategies such as membrane ultrafiltration or microfiltration [11–13, 18–20]. In this latter regard, the design of hybrid materials having large specific area, ease of handling, flexibility, physico-chemical inertness, and, of course, plenty of adsorption sites represents an open challenge towards obtaining increasingly efficient systems for decontaminating wastewater via batch adsorption/sequestration.

For this purpose, integrating nanocarbons and a flexible polymer into a fibrous architecture with tailored properties could be suitable for adsorbing and eventually detecting MB from stagnant water. As a polymer matrix, PVDF–HFP was selected by virtue of its appealing features, including mechanical robustness, thermal and photo-stability, electro-activity, and ease of processability [21, 22]. With respect to PVDF homopolymer, the introduction of HFP units endows the resulting PVDF-HFP copolymer with improved solu-bility, enabling the use of less toxic solvents like acetone, beyond imparting increased durability and higher tensile strength [23].

In fact, the integrity of polymeric substrate is manda-tory in order to avoid secondary pollution caused by the deterioration or disintegration of the sorbent during usage [1, 24]. As functional additives, two well-known nanocar-bons were chosen. Carbon nanotubes (CNTs) were used to provide active sites for the MB adsorption, by virtue of their extended sp^2 conjugated framework, and even to improve the mechanical and electrical performance of neat copoly-mer [13]. Graphene oxide (GO) was eventually added to endow the free-standing membranes with hydrophilicity and to assist CNTs in the adsorption of cationic dyes via multiple mechanisms, relying on electrostatic interactions, H-bonding, and π-π stacking [25].

Electrospinning was chosen as the processing technique, owing to the feasibility of fabricating thin yet robust mats capable of withstanding severe stresses while ensuring — when compared to other fabrication methods such as solvent casting and wet phase inversion — extremely larger values of specific surface, which are crucial prerequisites for the next-generation sorbent materials [1].

The current work was focused on investigating and eventu-ally maximizing MB adsorption, through isothermal and kinetic models, but even on monitoring how the structural and electrical features of the sorbents vary as a function of MB adsorption. In fact, while several studies report on the sorption performance of various materials, the investigation of the eventual evolution of structural and electrical features of the sorbents as they adsorb is still lacking in the scientific literature. For instance, the feasibil-ity to monitor the relationship between MB amounts recovered during the adsorption process and the electrical response of these materials may enable not only to control the state of the sorbents but even the reuse of exhaust sorbents as electronic devices.

2 Experimental part

2.1 Materials and preparative

GO (lateral size < 45 μm, thickness = 0.7–0.8 nm, C/O ratio = 1.1, density = 1.76 g/cm^3) was prepared by using Marcano and Tour's method. More details can be found in our previous reports [1, 26–29]. CNTs (length = 1–2 μm, diameter = 10–20 nm, C/O ratio = 40.7, density = 2.24 g/cm^3) were synthesized by fluidized bed chemical vapor deposition, according to our previous works [1, 26–29]. PVDF-co-HFP was a sample of Fluolyne HY purchased from CTS Europe. It is an elastomeric thermoplastic fluori-nated copolymer, having Mw = 400,000 g/mol and a density equal to 1.77 g/cm^3. Acetone and methylene blue (MB) rea-gent grade were purchased from Sigma Aldrich.

Electrospinning was carried out by using a conventional equipment (Linari, Italy) in a horizontal configuration and the following operating parameters were adopted: flow rate, 1.8 ml/h, supplied high voltage, 15 kV; needle-to-collector distance, 12 cm; temperature, 25 °C; relative humidity, 50%; electrospinning time, 2 h.

Prior to electrospinning, the polymeric solutions eventu-ally containing CNTs and/or GO were prepared via the ultra-sonication-aided dispersion of the nanoparticles in acetone, followed by polymer dissolution (10 wt% with respect to the solvent) under vigorous magnetic stirring. Four different com-positions, differing from each other for the amounts of fillers, were used to fabricate the samples, as listed in Table 1.

2.2 Characterizations

Scanning electron microscopy (SEM) was carried out by an ESEM FEI QUANTA 200. The samples were sputter-coated with gold before imaging to avoid electrostatic discharge during the test. AFM measurements were performed by a Multimode V (Veeco Metrology) scanning probe micro-scope, equipped with a piezoscanner, at room temperature, and under an N_2 atmosphere. More details can be found else-where. Atomic force microscopy (AFM) was also employed to measure the arithmetic (R_a) and squared mean (R_q) values of roughness.

Table 1 Formulation and codename of each sample

Sample codename	PVDF-co-HFP (wt%)	CNTs (wt%)	GO (wt%)
P-C0-G0	100	0	0
P-C2-G0	98	2	0
P-C2-G1	97	2	1
P-C2-G2	96	2	2

The rheological behavior of spinning solutions/dispersions in acetone was investigated by using a rotational rheometer (Mars, Thermofisher) in oscillatory frequency sweep mode using a 25-mm parallel-plate geometry. The tests were carried out at 20 °C at a constant strain amplitude (10%), within the frequency range of 5–100 rad/s.

Fourier transform infrared in the attenuated total reflection mode (FTIR/ATR) spectroscopy was performed to study the eventual structural evolution of the system after nanofiller(s) incorporation. Measurements were performed by using a FT-IR Spectrum 400 spectrophotometer (PerkinElmer) in the range 4000–450 cm^{-1}. The relative β fractions (F(β)) were quantified by using a well-established empirical relationship (Eq. 1):

$$F(\beta) = \frac{A_\beta}{A_\beta + 1.26 A_\alpha} \tag{1}$$

where A_β and A_α are the measured absorbance values at 836 and 763 cm^{-1} individually, and 1.26 is the ratio of absorption coefficients for β and α phases at their respective wavenumbers [30].

Electrical conductivity measurements were performed by using a Keithley 2440 source meter equipped with copper electrodes onto rectangular mats having length = 1 cm, width = 0.5 cm, and thickness ≃ 50 μm.

Water contact angle (WCA) testing was carried out to assess the surface character of membranes. Experiments were performed at room temperature by using an FTA 1000 (First Ten Ångstroms, UK) instrument. Deionized water (4 μL) was dropped onto the surface of each sample by way of an automatic liquid drop dosing system. Images of the drops onto the surface were acquired after 20 s.

2.3 Sorption tests

A total of 288 sorption experiments were conducted by varying the type of sorbent (P-C0-G0, P-C2-G0, P-C2-G1, P-C2-G2), the initial concentration (C_0) of MB aqueous solutions (1, 5, 10, 15, 25, 50 mg/L), and the contact time (0, 30, 60, 120, 180, 1440, 2880 min).

The sorption capacity of each sample was assessed by monitoring at predetermined time intervals the residual dye concentration via UV–vis spectroscopy, carried out in a UV–vis Specord 252 spectrophotometer (Analytik Jena, Jena, Germany). Absorbance values of the characteristic signals at $\lambda = 662$ nm were converted into concentrations by using opportunely constructed calibration lines, as already reported in our previous studies [1].

The time-dependent sorption capacity of materials, q_t, was evaluated by using the following equation (Eq. 2) [31]:

$$q_t = \left(\frac{C_0 - C_t}{W_s} \right) V \tag{2}$$

where C_0 and C_t are respectively the MB concentrations (expressed in mg/L) at the beginning of the experiment and at a given time; V is the volume of aqueous solution expressed in liters, whereas W_S is the weight of the sorbent expressed in grams.

At saturation, it is possible to define C_e and q_e, respectively, as the residual MB concentration and the sorption capacity of the sorbent achieved at equilibrium.

Sorption efficiency ($R\%$) was evaluated according to the following equation:

$$R(\%) = \left(\frac{C_0 - C_e}{C_0} \right) \times 100 \tag{3}$$

The equilibrium relationship between the adsorbent and the adsorbate is crucial to design an optimal adsorption process. As the adsorption capacity could be affected by the initial dye concentration, this aspect was elucidated, and Langmuir and Freundlich plots were constructed to fit the equilibrium adsorption data. The Langmuir model predicts that only a monolayer of adsorbent is supposed to adsorb and the total amount of adsorption capacity that is available to sites on the adsorbent is considered to be homogeneous and constant [11]. By contrast, Freundlich is an empirical model that relies on the consideration that multi-layer adsorption processes take place on heterogeneous surfaces [11].

The Langmuir model is defined by Eq. (4) [11]:

$$\frac{c_e}{q_e} = \frac{c_e}{q_m} + \frac{1}{q_m K_L} \tag{4}$$

The Freundlich model is expressed by Eq. (5) [11]:

$$\ln q_e = \ln K_F + \frac{1}{n} \ln c_e \tag{5}$$

where c_e (mg/L) and q_e (mg/g) are respectively the concentration of MB and the adsorption capacity of the sorbent at the equilibrium, q_m is the maximum adsorption capacity under ideal conditions, n is an empirical parameter correlated with the adsorption capacity, whereas K_L and K_F respectively indicate the constants of Langmuir and Freundlich equations.

However, equilibrium studies do not provide much insight about the adsorption mechanism and rate. In fact, the movement of solute across the boundary depends on the physicochemical features of the given sorbent. In order to investigate this solute partitioning, a detailed study about the process rate and the rate-limiting step such as mass transport and chemical reaction processes is mandatory. Four different kinetic models, namely pseudo-first order (PFO), pseudo-second order (PSO), Elovich, and intra-particle diffusion (IPD) models were employed to fit the experimental data, according to the equations listed in Table 2.

Table 2 Equations of kinetic models and regression methods for determining parameters [2, 11, 31]

Model	Equation		Regression methods
PFO	$q_t = q_e(1 - e^{-k_1 t})$	(6)	Plot: $\ln(q_t - q_e)$ vs t slope $= -k_1$; intercept $= \ln q_e$
PSO	$\frac{t}{q_t} = \frac{1}{kq_e^2} + \frac{1}{q_e}t$	(7)	Plot: t/q_t vs t slope $= \frac{1}{Q_e}$; intercept $= \frac{1}{kQ_e^2}$
Elovich	$q_t = \frac{1}{\beta}\ln t + \frac{1}{\beta}\ln(\alpha\beta)$	(8)	Plot: q_t vs $\ln t$ slope $= \frac{1}{\beta}$; intercept $= \frac{1}{\beta}\ln(\alpha\beta)$
IPD	$q_t = k_{IPD}t^{0.5} + C_{IPD}$	(9)	Plot: q_t vs $\sqrt{t}$ slope $= k_{IPD}$; intercept $= C_{IPD}$

The PFO model is expressed by Eq. (6), where k_1 is the rate constant of adsorption (min^{-1}). Whether the sorption process has one limiting step, the plot of $\log(q_e - q_t)$ against t would give a linear relationship that allows calculating k_1 and q_e from the slope and intercept of the plot, respectively.

PSO (Eq. 7) describes sorption processes whose kinetic rate is limited by two steps. In this latter case, the parameters of its non-linear form, i.e., the rate constant of adsorption, k_2 (g/mg min), and q_e can be determined by plotting t/q_t as a function of t.

In the Elovich model (Eq. 8), α is the initial adsorption rate (mg/g min) and β is the desorption constant (g/mg). The plot of q_t against ln t provides a linear relationship in the case of chemical adsorption processes, and α and β are can be determined from the slope and intercept of the plot.

Whether the limiting step of an adsorption process is represented by the mass transfer, the IPD model (Eq. 9) enables accounting for film diffusion and/or intra-particle diffusion, whose characteristic parameters, namely the constant rate, k_{IPD} (mg/(g min$^{0.5}$)), and the contribution of initial surface adsorption, C_{IPD} (mg/g), can be determined by examining the slope and the intercept of multilinear lines.

2.4 Sensing tests

To evaluate the sensing performance of these materials, electrical measurements were carried out using a custom-built setup comprising an Arduino board equipped with Serial Plotter software within the Arduino IDE. Additional details, including the scripts employed, can be found in the Supporting Information (SI).

3 Results and discussion

The viscosity of solutions plays a crucial role in the electrospinning process [32, 33]. Furthermore, in complex systems involving polymer, solvent, and various nanofillers, the rheological behavior serves as an indicator of nanofiller dispersion, also providing insights into the nanoarchitectures formed through the self-assembly capabilities of two distinct types of nanoparticles [32, 33]. The rheological analysis of spinning solutions/dispersions, provided in Fig. 1, revealed remarkable non-Newtonian behavior across all systems. Expectedly, the viscosity increased with the addition of 2% CNTs (P-C2-G0). The introduction of 1% GO (P-C2-G1) resulted in the highest viscosity values across the frequency range, while 2% GO (P0-C2-G2) surprisingly led to decreased viscosity, yet remained higher than that of P-C0-G0 solutions. This peculiar behavior can be attributed to several and contrasting factors, including the unique viscoelastic properties of GO dispersions, which vary with concentration [34]. While having the ability to align during flow, GO layers can either constitute a hybrid GO-CNT interconnected network at a lower dose — with restriction of mobility and solid-like behavior — or entrapping CNTs onto their basal planes [35] thus enhancing fluidity at a higher dose. Moreover, the presence of 2% GO delays solvent evaporation, maintaining fluidity for a longer duration compared to other samples, with this peculiar feature of GO being elucidated in previous works [29, 36]. Despite these variations, all systems exhibited favorable characteristics for electrospinning, boasting adequate viscosity levels and distinctive non-Newtonian behavior.

The morphology of the mats was investigated by integrating SEM and AFM analyses, whose outcomes are provided in Fig. 2. Neat polymer (Fig. 1a, e, i, m) displays a grid-like configuration where it is possible to observe the presence of fiber junctions caused by the absence of non-solvent during
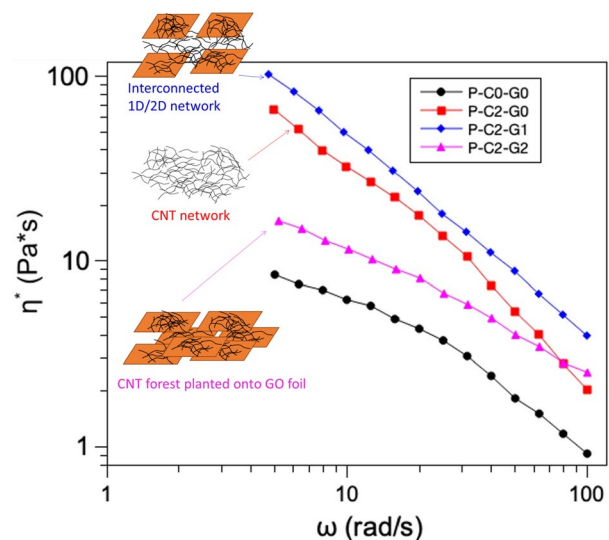

Fig. 1 Rheological analysis of spinning solutions/dispersions together with schematics of possible nanoarchitectures formed through self-assembly of nanofillers
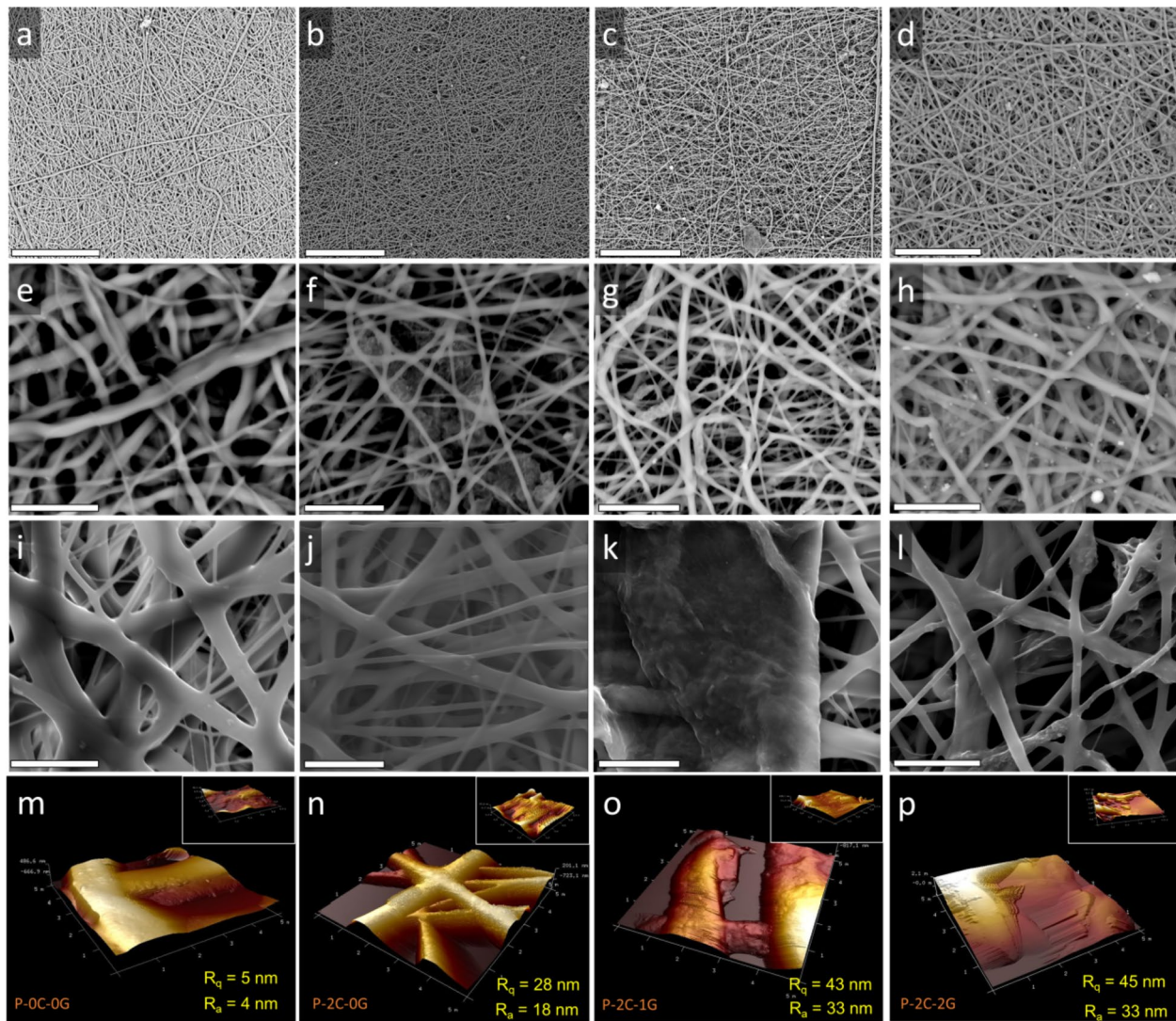
Fig. 2 Morphology of the mats prepared. SEM micrographs at different magnifications of P-C0-G0 (**a**, **e**, **i**), P-C2-G0 (**b**, **f**, **j**), P-C2-G1 (**c**, **g**, **k**), P-C2-G2 (**d**, **h**, **l**). Scale bars: 20 µm (**a–d**), 10 µm (**e–h**), 5 µm (**i–l**). AFM images of squared regions (5 µm × 5 µm) along with the detailed views (1 µm × µm) used to calculate squared mean (Rq) and arithmetic average (Ra) roughness, provided as insets, for P-C0-G0 (**m**), P-C2-G0 (**n**), P-C2-G1 (**o**), and P-C2-G2 (**p**)

electrospinning. Such a randomly oriented crosslinked network of fibers showed bimodal size distribution (Fig. S1) and a very smooth texture.

P-C2-G0 (Fig. 2b, f, j) substantially retains similar morphology, although the fibers proved to be thinner because of the introduction of conductive fillers in the electrospinning solution, and a bad filler dispersion (see Fig. 2f), reasonably due to the scarce dispersibility of CNTs in acetone. AFM analysis (Fig. 2n) reveals that in this case, the fibers evolve into a brush-like structure, with a forest of CNTs protruding out of polymeric fibers. This occurrence was likely responsible for the 400% increase of roughness if compared to neat polymer. The images of P-C2-G1 and P-C2-G2 are respectively reported in Fig. 2c, g, k, o, d, h, l, and p. A hybrid integration of CNTs and GO, while not altering significantly some features of mat architecture, such as the orientation and size distribution of fibers, resulted in a variegated microstructure. In fact, in both hybrid samples, the surface localization of nanoparticles was observed at larger extents, as confirmed by detailed micrographs of Fig. 2k and m, where it is possible to note GO foils emerging from the surface of the samples P-C2-G1 and P-C2-G2, respectively. Obviously, this occurrence led to a rougher texture, with both samples displaying the highest values of Rq and Ra (i.e., respectively 8 times and 2 times higher than those of neat polymer and P-C2-G0). Noteworthy, no significant differences in terms of roughness were detected among the two hybrid nanocomposites, despite a different GO dosage.

The outcomes of FTIR/ATR analysis are reported in Fig. 3. The polymorphism of vinylidene fluoride part of PVDF-co-HFP copolymer can be investigated via FTIR/ATR spectroscopy, as thoroughly and extensively reported elsewhere [37]. In fact, vibrational bands of α phase are located at 530 cm^{-1}, 615 cm^{-1}, 765 cm^{-1}, and 795 cm^{-1}, while vibrational bands exclusively of β phase can be detected at 510 cm^{-1} and 840 cm^{-1}, and the bands related to the γ phase are located at 431 cm^{-1}, 776 cm^{-1}, 812 cm^{-1}, 833 cm^{-1}, and 1233 cm^{-1} [37]. At first glance, the spectra of materials appear very similar. However, a deeper analysis of the region 1000–500 cm^{-1} revealed some differences in the crystallinity of the vinylidene fluoride part of the fluorinated copolymer.

Fig. 3 FTIR/ATR spectra in the full wavenumber region (**a**) and in the range 1000–500 cm^{-1} for the detection of beta and alpha phases
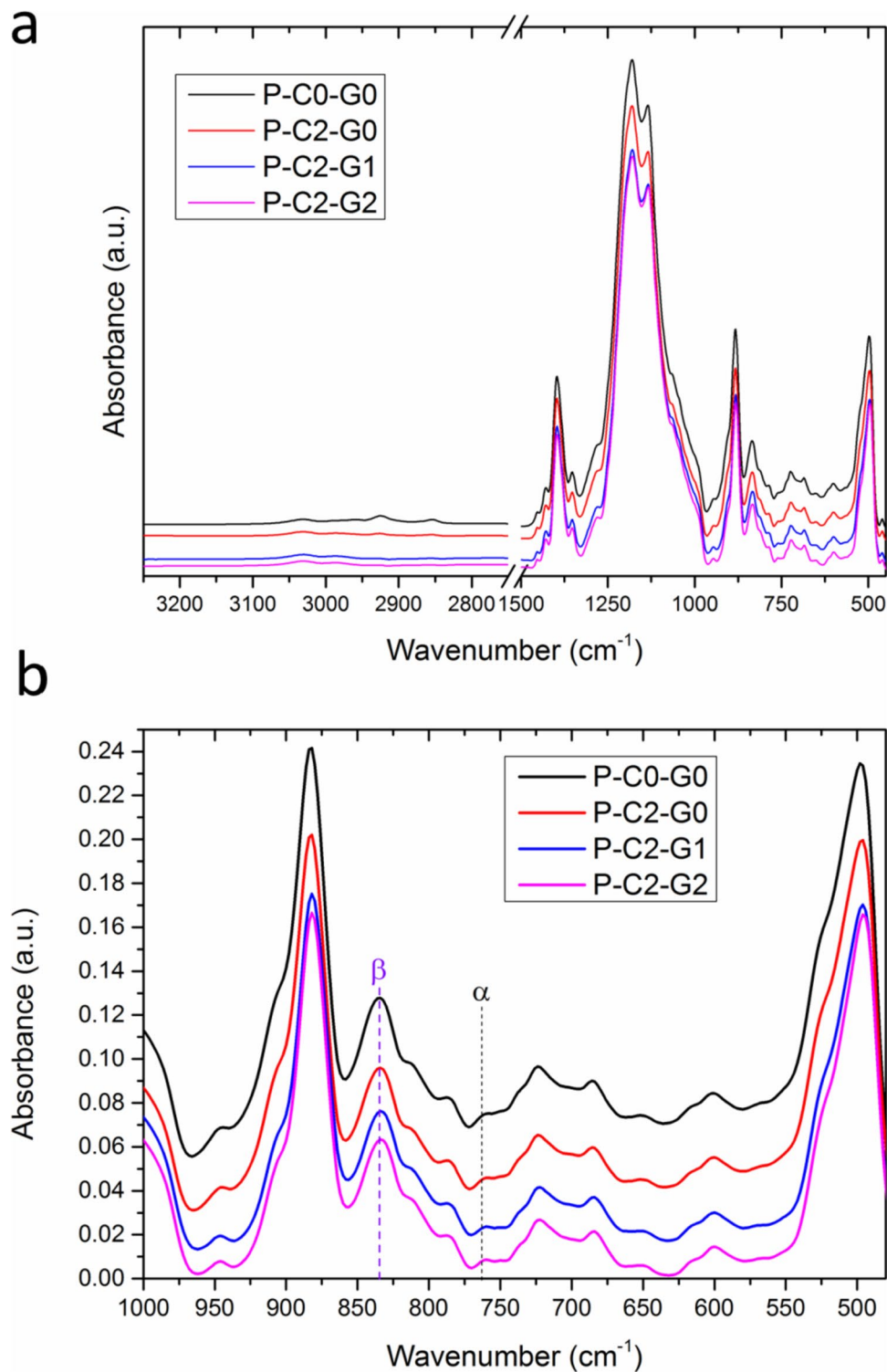
The relative fraction of the electroactive beta phase, already quite high in the neat matrix due to the electrical field and elongational flow induced by electrospinning, is even enhanced by integrating nanoparticles, with a maximum observed for P-C2-G2 (see the first row of Table 3). This behavior, consistent with what is reported in the scientific literature, is typically ascribed to the synergistic effect of electrospinning and nanocarbons [38–41].

Other salient features of the mats, including electrical properties and wettability, are listed in Table 3. The results of electrical tests show that the highest conductivity was exhibited by P-C2-G0, whereas integrating a semiconductor such as GO at either 1% or 2% did not exert any synergistic effect with CNTs. Likewise, this occurrence can be explained by considering that in the absence of GO, CNTs are badly dispersed and this feature leads to the formation of segregation patterns in which CNTs are confined, and they are able to touch each other, thus giving rise to a conductive network.

On the other hand, GO addition promotes the dispersion throughout the matrix of CNTs, which were even found to be planted onto GO foils. In this latter arrangement, electrical conductivity can be guaranteed by a tunneling effect, which is less efficient [42]. Furthermore, the electrical conductivity of GO is known to be affected by the degree of oxidation, since oxygenated moieties hinder the electron transport throughout the graphene sp^2-conjugated framework, thus providing GO with a capacitive behavior [42–44]. Hence, the electrical conductivity of nanohybrid mats proved to be 4 or 5 orders of magnitude lower than that of P-C2-G0, yet dramatically higher than that of neat PVDF-HFP.

On the contrary, the hydrophilic character of the mats proved to enhance upon GO content, likely owing to the well-known wettability of extremely oxidized GO sheets and by virtue of their surface localization. The large surface-specific area of such mats, along with the presence of CNTs and GO that are excellent active sites for the adsorption of many pollutants could make these materials particularly suitable for water treatment applications. As a proof of concept, MB was selected as a model dye and it was evaluated the influence of various parameters, including formulation of the samples, contact time, and initial MB concentration, onto the MB removal performance of the materials, as provided in Fig. 4.

The data point out that, regardless of MB concentration and contact time, the sorption curves of nanocomposites increase steadily and monotonically within the first stage of

the experiment, while gradually plateauing at longer times, until a sorption equilibrium (q_e) is reached. This behavior can be interpreted based on the availability of vacant active sites on the surface of the mats that are mainly occupied during the first hours [11]. Afterwards, there are no sufficient active sites on the adsorbent to adsorb MB molecules, thus the adsorption properties increased slowly. Of course, the values of q_e and t_e, namely the adsorption capacity at equilibrium and the corresponding time required, depend on the different contents of active nanoparticles bearing onto the surface of the various sorbent systems with respect to the initial concentration of the pollutant, since P-C0-G0 sample showed negligible sorption capacity in all the testing conditions.

In this latter context, in the whole C_0 range investigated, the following order is retained in terms of q_e: P-0C-0G < P-2C-0G < P-2C-1G < P-2C-2G. Despite this, however, at the lowest MB content ($C_0 = 1$ mg/L) plateau is achieved faster (within 180 min for P-2C-2G, 1440 min for the other sorbents), whereas at higher values of C_0, longer contact times are required (up to 3800 min in some cases) for the plateauing of the sorption curves. This aspect implies that when MB molecules are relatively few in number, they are more rapidly adsorbed onto the most available active sites of the sorbent, while above a certain MB content, the adsorption process involves less accessible binding sites of the sorbent, such as inner cavities and smaller pores originated by the arrangement of nanoparticles and polymers in the hierarchical structures. Predictably, as the initial MB content increases, the adsorption capacity at the equilibrium (q_e) proved to increase, while the removal efficiency ($R\%$) of the systems was found to decline, although at different extents, as shown in Figure S2. This could be clearly explained by considering that upon increasing dye concentration, it tends to augment the driving force to allow the mass transfer among the liquid and solid phases, but, conversely, the binding sites of the sorbents tend to be progressively saturated, thus resulting in a reduced efficiency [11].

Isotherm models were used to describe how the MB molecules distribute between the liquid phase and the solid phase when the adsorption process reaches an equilibrium state. The parameters obtained from the two models give useful information about the surface property and affinity of sorbent systems. The equilibrium data of the three samples, Fig. 5, constructed at the six different initial concentrations of MB previously discussed (1–50 mg/L), displayed a different behavior of q_e as a function of c_e. The lower R^2 coefficients of the Freundlich model (see Table 4) indicate that this equation is not able to fit isotherm data. Otherwise, the Langmuir model proved to be particularly suitable for interpreting experimental data of the samples, especially in the case of neat polymer and hybrid mats (R^2 values higher than 0.99). These outcomes suggest that the MB adsorption can be regarded as a monolayer process.

Table 3 Physicochemical characteristics of the samples investigated

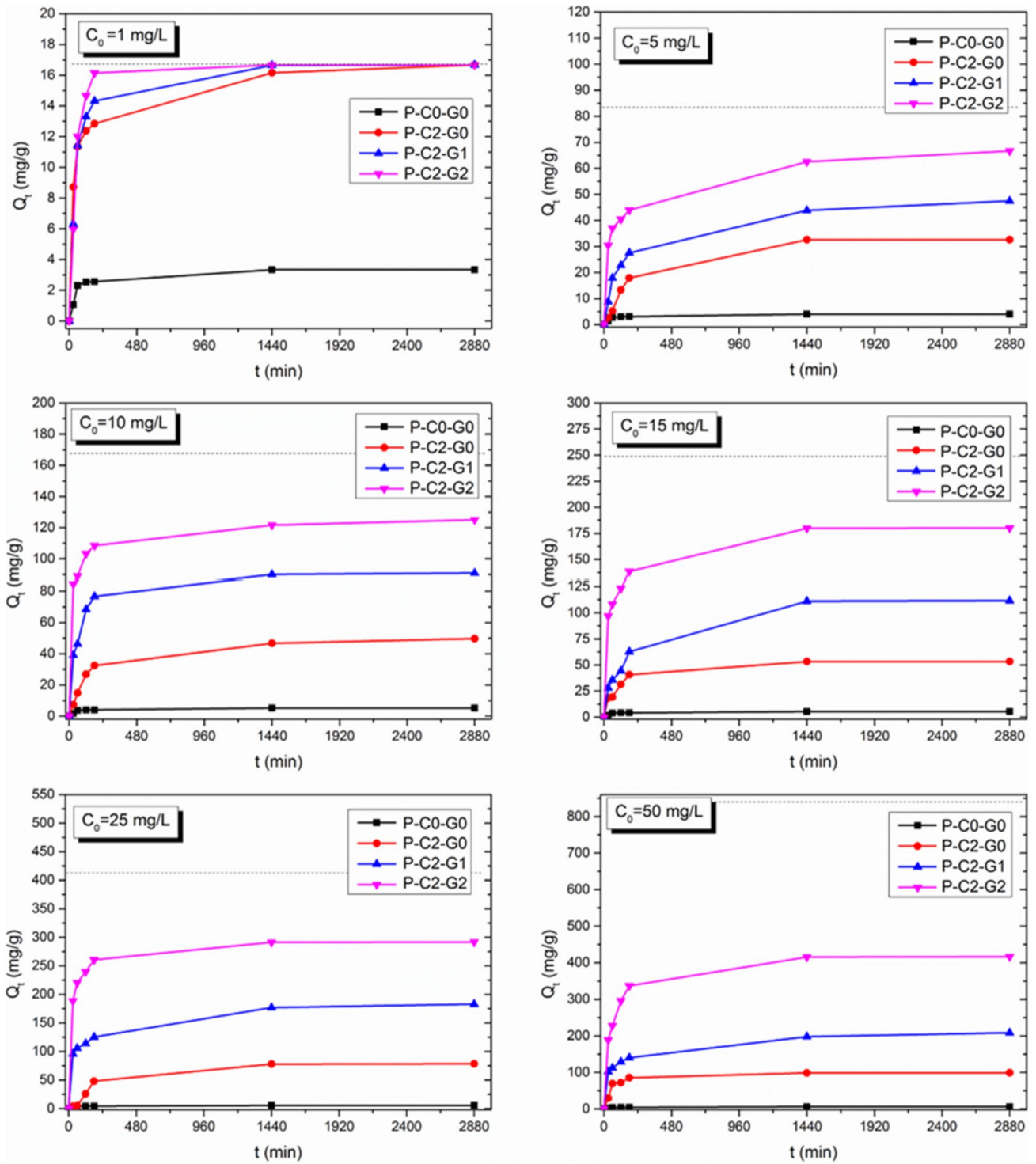|	P-C0-G0	P-C2-G0	P-C2-G1	P-C2-G2
Beta function	0.678	0.780	0.771	0.857
σ (mS/m)	$< 10^{-6}$	33.33	7.21×10^{-3}	1.25×10^{-3}
WCA (deg)	110	121	92	78

Fig. 4 Time-dependent adsorption capacity of the systems at different initial concentrations of MB solutions
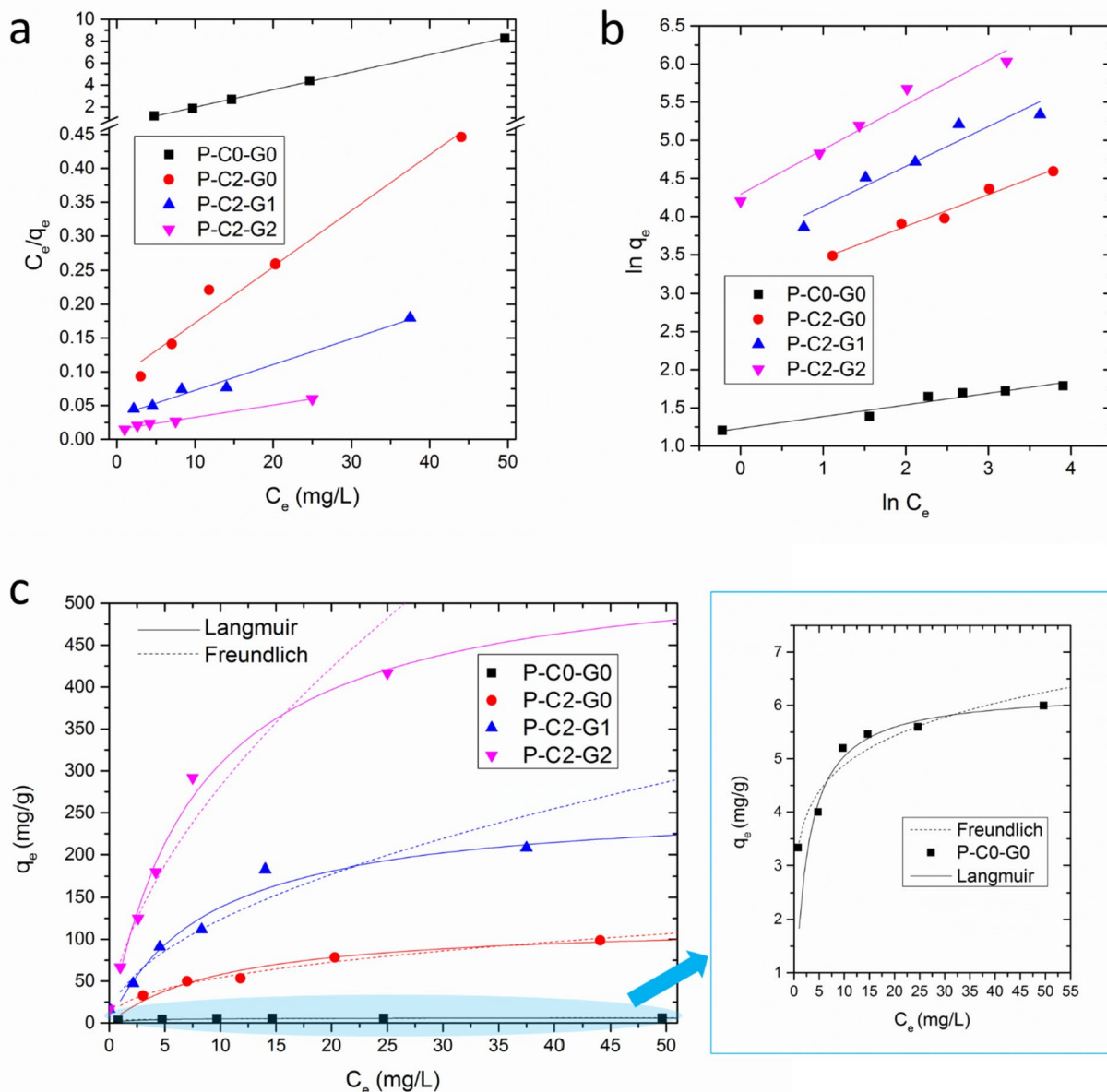
Fig. 5 Fitting plots using linearized forms of Langmuir (**a**) and Freundlich (**b**) equations; comparison between experimental data and theoretical predictions of non-linear Langmuir (solid lines) and Freundlich (dashed lines) isotherm models (**c**)

More interestingly, the Langmuir equation allows assessing also the maximum dye adsorption capacities of P-C0-G0, P-C2-G0, P-C2-G1, and P-C2-G2, which were found to be respectively equal to 6, 120, 263, and 555 mg/g. These values stand out significantly in comparison to those observed in other highly promising electrospun mats, as illustrated in

Table 4 Fitting results of Langmuir and Freundlich isotherms

Sample	Langmuir			Freundlich		
	q_m	K_L	R^2	n	K_F	R^2
P-C0-G0	6.272	0.4120	0.9994	6.5155	3.4286	0.7037
P-C2-G0	120.48	0.0923	0.969	2.3976	20.827	0.9409
P-C2-G1	263.16	0.1105	0.9764	2.067825	37.016	0.8055
P-C2-G2	555.56	0.1250	0.9925	1.892864	73.109	0.903

Fig. 6. More in detail, Fig. 6a provides a comparison among various electrospun membranes prepared by incorporating active compounds in the bulk. In particular, the q_m (mg/g) of each system is plotted as a function of the weight content of active compound incorporated in the polymer matrix. Our systems gave excellent results, especially considering the small amount of active nanoparticles (2–4%) incorporated in a scarcely active matrix such as PVDF-co-HFP. In fact, the sorption capacity values of such hybrid nanocomposites largely exceed those predicted by the linear combination of the concentrations of starting components, according to the mixture law. Note that, although the volume content of neat polymer in the three different nanocomposites is ca. 96–98%, the sorption capacity of these latter proved to augment from 20 (P-C2-G0) to almost 100 times (P-C2-G2), thus showcasing a performance twice as impressive as that of materials containing more commonly used active polymer substrates, such as polyethersulfone and polyacrylonitrile, along with a greater quantity of active nanoparticles.

Furthermore, as depicted in Fig. 6b, our results overcome even those achieved by electrospun systems with either a shell or a uniform coating of active compounds.

Given the remarkable results achieved, it is crucial to delve into the underlying absorption mechanism and comprehend the interactions among the components of such nanohybrid materials that led to the activation of a substrate that, by itself, exhibited minimal affinity for MB. It is well-known that when MB is adsorbed on graphene domains via π-π interactions, each molecule is arranged in parallel stacking on the nanocarbon plane, while in the oxygenated domains of GO, the binding involves nitrile groups of the MB molecules, which are arranged vertically. The latter configuration enables the sorbent to adsorb larger quantities of MB before saturating the active sites. This aspect implies that the sorption capacity of GO tends to exponentially augment upon increasing its oxidation degree, reaching the value of approximately 1000–1200 mg/g for the extremely oxidized samples. CNTs, bearing a cylindrical surface with
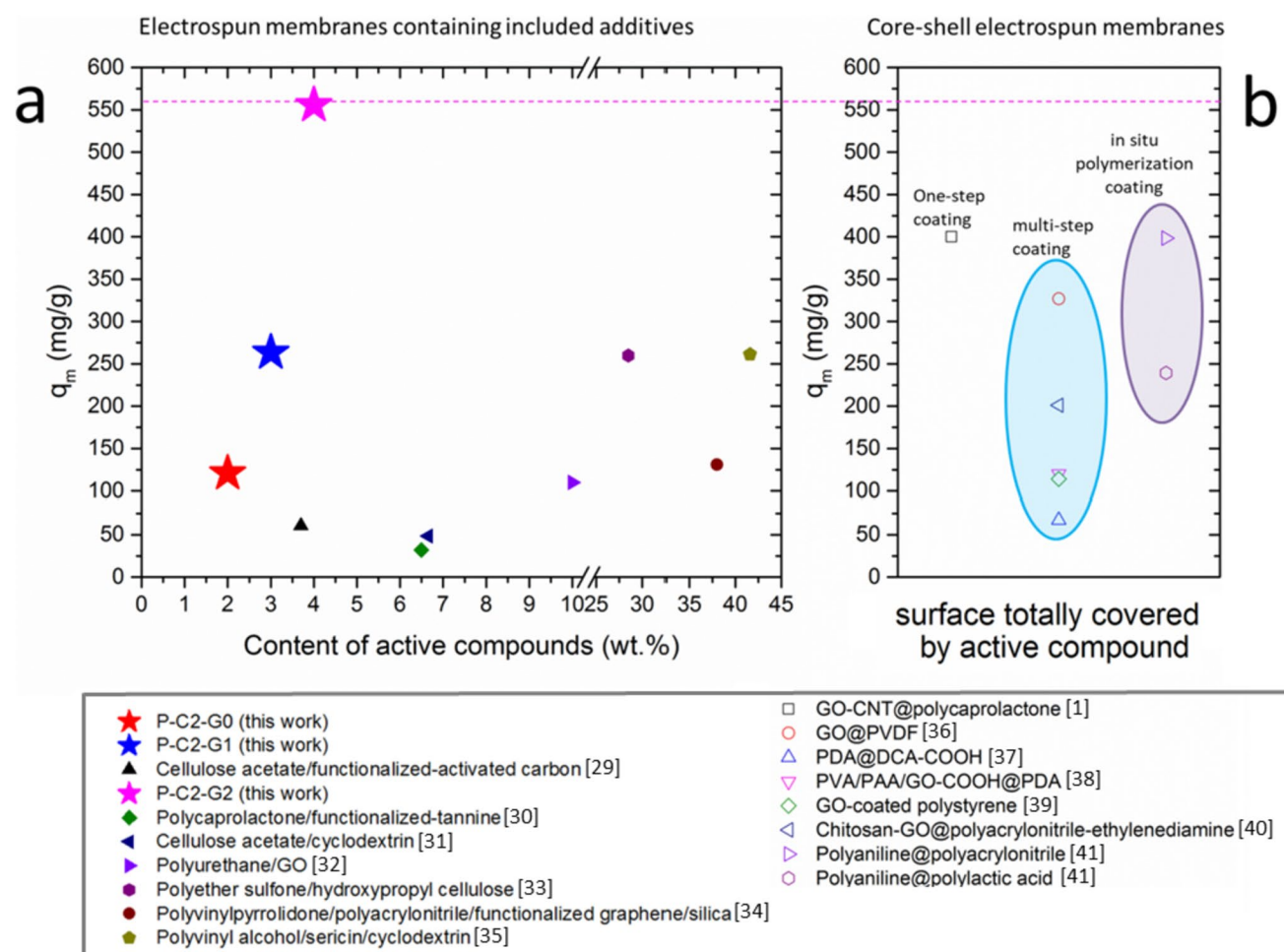

Fig. 6 Comparison between the sorption performance of the materials proposed in this work and various electrospun mats, either modified by incorporating active compounds in the bulk [45–51] (**a**) or in the surface [1, 52–57] (**b**)

an aromatic sp² framework, have a typical MB sorption capacity in the order of 90–100 mg/g, ascribed to π-π stacking and electrostatic interactions, owing to its negative zeta potential. Furthermore, it was reported that sp² carbonaceous materials tend to have a Freundlich-type behavior, whereas oxidized nanocarbons follow a Langmuir-type behavior. PVDF-co-HFP, on the other hand, has a proven affinity to MB molecules, ascribed to the PVDF part of the copolymer, with a reported binding energy equal to -128.7 kJ mol^{-1} [58]. However, its smooth surface results in a relatively low surface area that affects sorption capacity.

The mechanism of adsorption was investigated by using four kinetic models, namely, pseudo-first order (PFO), pseudo-second order (PSO), Elovich, and intraparticle diffusion (IPD) models. For the sake of brevity, we report the results of the sorbent systems operating at $C_0 = 25$ mg/L. As one can see from the results reported in Fig. 7 and Table S1, the PFO equation is able to describe the sorption kinetics of the P-C2-G0 system, while providing low accuracy in data fitting of the other samples that, on the contrary, are matched by the PSO equation. Indeed, it was previously reported that nanocarbons may change their
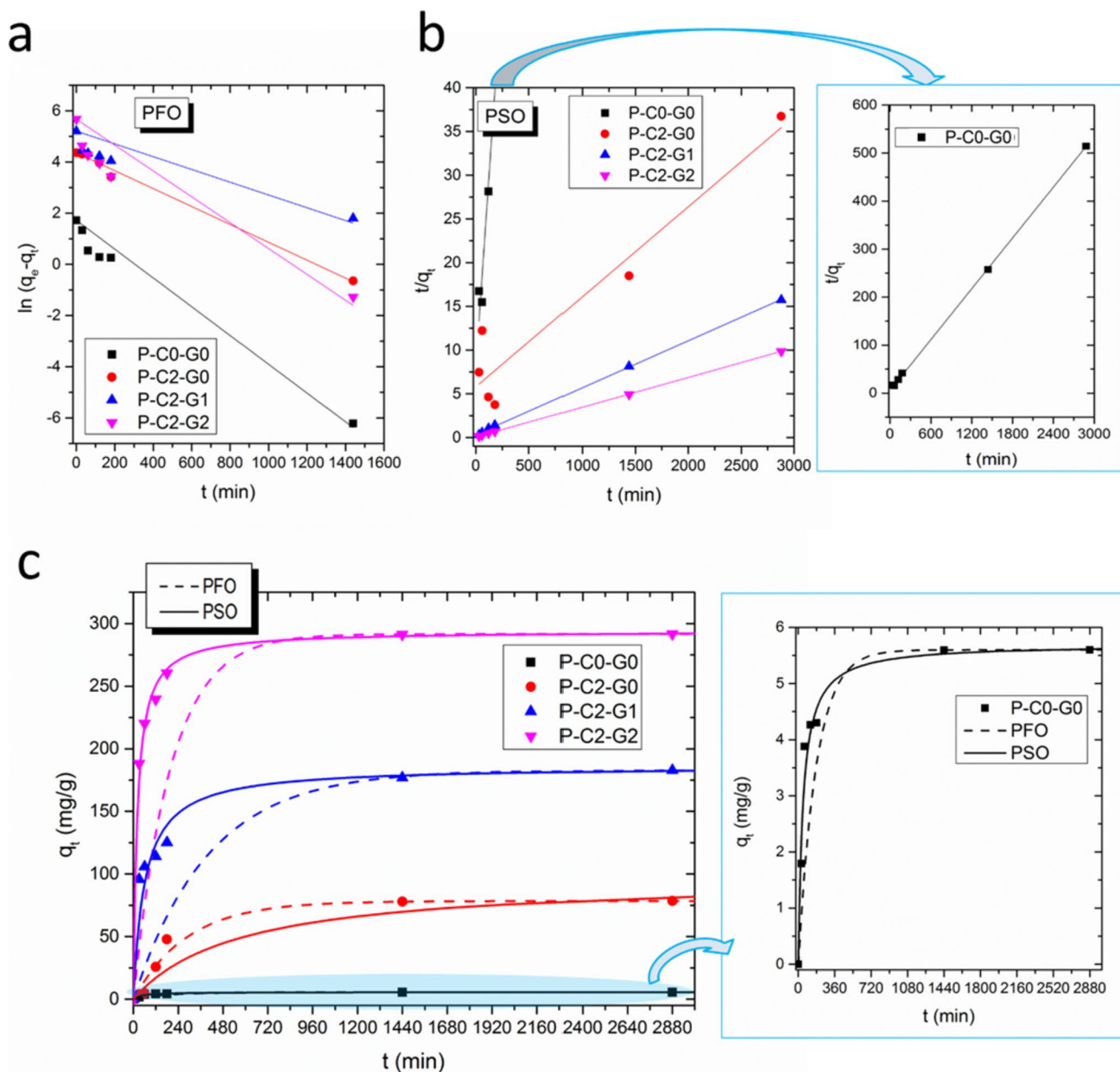
Fig. 7 Comparison between experimental data and theoretical predictions of the linearized forms of PFO (**a**) and PSO (**b**) and non-linear form of both models (**c**)

sorption behavior from PFO- to PSO-type depending on their oxidation degree.

It is well-known that heterogeneous adsorption is governed by surface adsorption and diffusivity, with these features being influenced by morphological parameters, including the volume and dimensions of pores, surface area and therefore availability of active sites, as well as by physicochemical aspects, such as the wettability of the structures and the extent and type of electrostatic or π-π* interactions between adsorbent and adsorbate. P-C2-G0, P-C2-G1, and P-C2-G2 systems differ from each other not only in terms of overall concentration of active nanoparticles (i.e., GO amount, being constant the CNT content) but even in a structural organization, with hybrid mats bearing a higher content of surface-localized nanoparticles which inevitably

increased their wettability (Table 3), and thinner diameters (Fig. S1), which may result in larger values of surface area.

The eventual chemical nature of the adsorption process can be elucidated by the Elovich model. As visible in the results of data fitting, provided in Fig. 8a and Table S2, this latter model provides fair accuracy to fit hybrid systems, while being totally unable to describe the behavior of P-C0-G0 and P-C2-G0. In fact, it is well-established that unlike CNTs and neat polymer, GO nanoparticles tend to adsorb MB molecules by exploiting a combination of physisorption and chemisorption, where the formation of either π-π* or ionic complexes, H-bonding and electrostatic interactions are all involved [59].

Aiming to assess the role of diffusivity in the sorption process, the IPD model was implemented, too. The data, provided in Fig. 8b and Table S2, highlighted that this model is able to
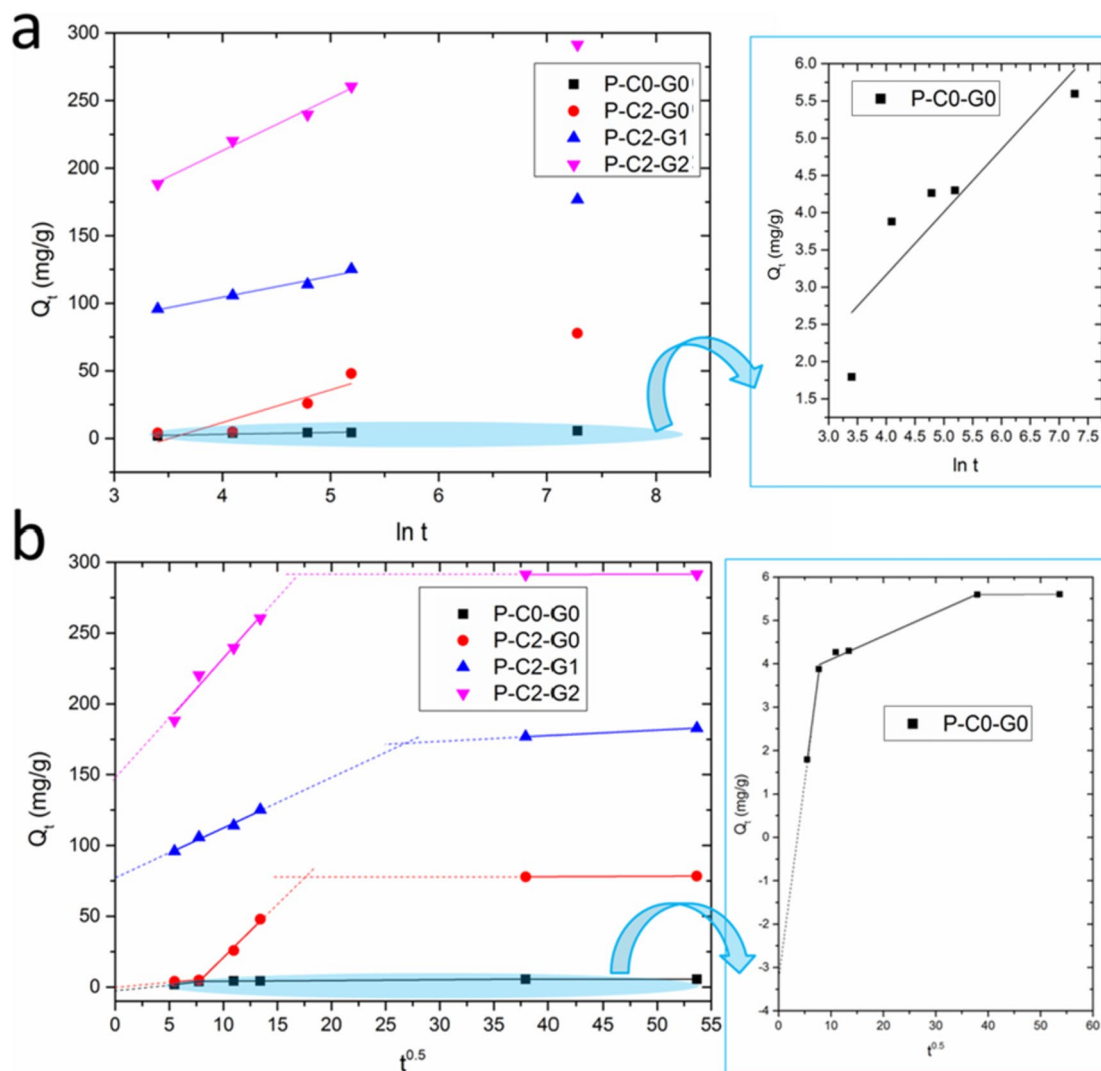

Fig. 8 Comparison between experimental data and theoretical predictions of the Elovich model (**a**), fitting plots of the IPD model along with characteristics of the initial adsorption process (**b**)

describe the sorption behavior of all the samples, especially P-C2-G0 (correlation coefficient $R^2 > 0.995$). Noteworthy, all the materials display multi-linear plots, with two or three steps being involved to follow the whole process, thus indicating that multiple steps take place during adsorption [60, 61]. P-C0-G0 and P-C2-G0 display three distinct regions, hybrid mats only two. The first section of the curve refers to the so-called film diffusion, that is, the mass transfer from the bulk solution to the external surface of membranes [60, 61].

The second zone describes the gradual adsorption stage, corresponding to the diffusion of the MB molecules from the external surface into the pores of the nanoparticles (intra-particle diffusion) [60, 61]. The last section, generally characterized by a small slope, indicates the final equilibrium stage, in which the solute moves slowly from large pores to micropores [60, 61]. Moreover, the first section of such plots provides information about the initial adsorption behavior. If the straight line passes through the origin, the film diffusion is the only rate-limiting step. Otherwise, it could be found either a negative or positive intercept, respectively indicating an unfavorable or rapid film diffusion, respectively. According to this model, in the initial linear stage of adsorption, the slope (K_{IPD}) and the intercept (C_{IPD}) of the fitting lines provide information about the rate constant and the initial adsorption behavior of systems, respectively. In particular, the parameter accounting for the initial characteristic of the curve is named R_i, which is expressed as:

$$R_i = 1 - \frac{C_{IPD}}{q_e}$$

where, of course, q_e is the maximum sorption capacity at the equilibrium. R_i generally varies from 0 to 1, with the former value being representative of a completely initial adsorption and the latter describing the absence of initial adsorption [60]. In some rare cases, R_i might be even higher than 1, thereby indicating the existence of external mass transport resistance that renders unfavorable the film diffusion [61].

Data analysis pointed out that P-C0-G0 belongs to the latter category, likely due to the combination of hydrophobic character, smooth surface, and large fiber diameter, which make the initial film diffusion particularly problematic. On the other hand, film diffusion proved to be the rate-limiting step in the case of the hydrophobic P-C2-G0, which displayed $C = 0$ (and therefore $R_i = 1$). In this case, the straight line passing through the origin showed a small slope, thus indicating a slow transport of MB from the bulk solution to the external surface of the sorbent by film diffusion, presumably because of the hydrophobic character of the sample. The progressive increase of GO content from 0 to 2% resulted in an increase of both K_{IPD} and intercept values. R_i was found to be close to 0.5 for both hybrid systems, thus indicating an intermediately/strongly initial adsorption, prompted by the enhanced wettability provided by GO.

This feature suggests that intra-particle diffusion is the limiting step of the adsorption process for the P-C2-G0 sample, which in fact follows a PFO mechanism, while it is not the only factor affecting adsorption for all the other materials, thus providing further evidence that the other systems follow a PSO mechanism. Despite this, the fitting lines for the four systems were found to be almost parallel in the last zone, which describes the situation close to saturation, while remarkable differences were found in the early stage of adsorption. Hence, the different wettability of the systems and the different content and dimensions of pores within the structures might have played the most crucial role in the whole sorption performance.

Aiming at a deeper comprehension of eventual structural changes imparted by MB adsorption to the polymer matrix, and to study the type of sorbent-sorbate interactions, FTIR spectroscopy was performed onto the samples before and after the sorption tests, and the spectra were compared with that of MB (Fig. 9).

After adsorption, P-C0-G0 and P-C2-G2 displayed a broad band at roughly 3400 cm^{-1} and at 1666 cm^{-1}, otherwise not detected. These spectral features could be ascribed to the N–H bond of MB molecules. Notably, the signal at 1608 cm^{-1} (C = N central ring stretching of MB) disappeared in all the samples after MB conjugation, providing further evidence of the strong π-π interactions involved. Bands centered at 1340 cm^{-1} and 1481 cm^{-1}, respectively related to the C = N stretching and C = C side ring stretching [62], are observed only in the spectra of MB and MB–P-C2-G2 complex, which was the only case in which the typical modes of sorbent and sorbate were found to either overlap or recombine. This aspect may suggest that also the polymer is directly involved in the sorption, in full agreement with the large extents of sorption achieved, despite the small amounts of fillers used.

Hence, we can conclude that MB sorption imparts in all the cases significant structural changes, although some differences were found among the samples, likely correlated to the prevalence of vertical or parallel binding of MB molecules, in full agreement with the results of equilibrium isotherms. Indeed, under the considerations that MB has a remarkable conductivity ($\simeq 100$ S/cm) [63] and that MB-CNT complexes proved to increase the content of electroactive crystalline phases of PVDF [38], it could be hypothesized that the larger the amount of MB adsorbed, the higher the electrical conductivity of the system. All the sorbents used in the experiments were then subjected to electrical measurements. The results, plotted in Fig. 10a, point out that all samples experience a progressive increase in their electrical conductivity as they absorb MB. Although P-C2-G0 displayed the worst performance as a sorbent system, its electrical properties ($\sigma = 33.33$ μS/cm) proved to be dramatically
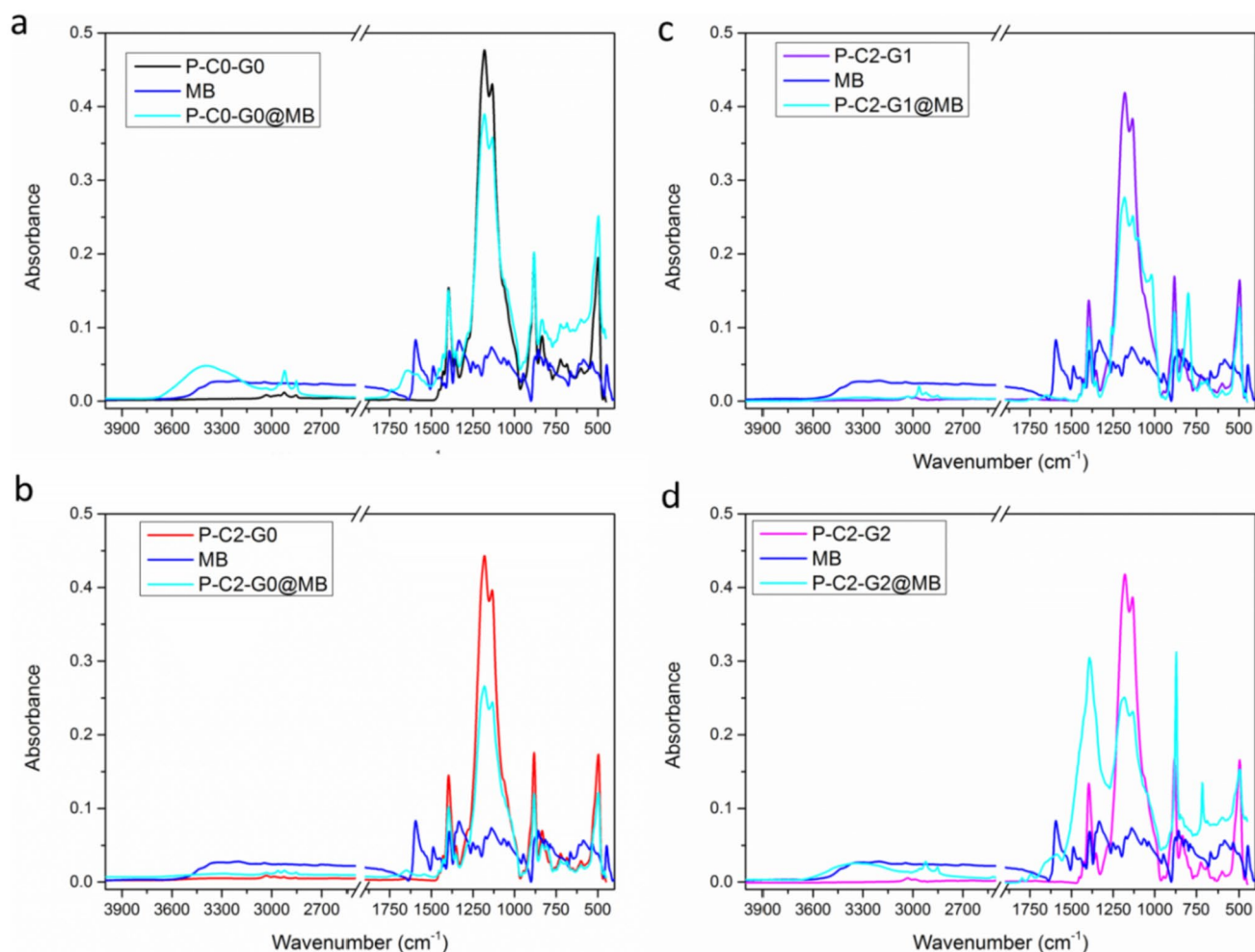
Fig. 9 FTIR/ATR spectra of P-C0-G0 (**a**), P-C2-G0 (**b**), P-C2-G1 (**c**), and P-C2-G2 before and after MB adsorption, along with MB as a reference plot

higher than those of nanohybrid systems, both before and after adsorption. The values of electrical conductivity were then plotted as a function of the amount (milligrams) of MB adsorbed, and the outcomes are reported in Fig. 10b. Notably, a linear trend was found with a high sensitivity (ca. 309 $\mu S\ cm^{-1}\ mg^{-1}$) in the first range of MB amount adsorbed (below 0.235 mg), which enables these samples as detectors for small amounts of MB dissolved in water. Thereafter, when the MB amount adsorbed is close to the highest admissible value (i.e., 0.36 mg, according to the Langmuir model), CNT sidewalls, inner cavities, and pores are about to be saturated and the electrical conductivity jumps from 102 to 150 $\mu S/cm$. Substantially, the same trend was found for P-C2-G1 (Fig. 10c) and P-C2-G2 (Fig. 10d), although with progressively lower sensitivity and shorter linear range.

In fact, all of these systems show the typical percolation behavior of composites. As the amount of MB adsorbed increases, the tunneling distance is reduced, more conductive pathways are formed, until a percolation threshold is achieved. Of course, depending on the extent of surface sites covered with MB molecules, along with the vertical or parallel arrangement of dye molecules, the saturation percolation threshold may vary. This latter aspect could be likely explained by considering that materials containing solely CNTs, tend to adsorb MB molecules by parallel stacking; hence, the saturation of sites occurs before, and electrical conductivity tends to increase with a higher slope. Otherwise, when the progressively augmenting content of GO implies a certain aliquot of MB molecules vertically bonded, this property is apparently less influenced by adsorbed MB amount. Aiming to get rid of this feature, the evolution of electrical conductivity was plotted as a function of the fraction of surface sites covered with MB, using the highest admissible value (q_m) predicted by the Langmuir model for each sample, and provided in Fig. 11.

As one can see, when plotted against the surface coverage degree (q/q_m), the behavior of conductivity proved to be similar for all the samples, with a percolation threshold
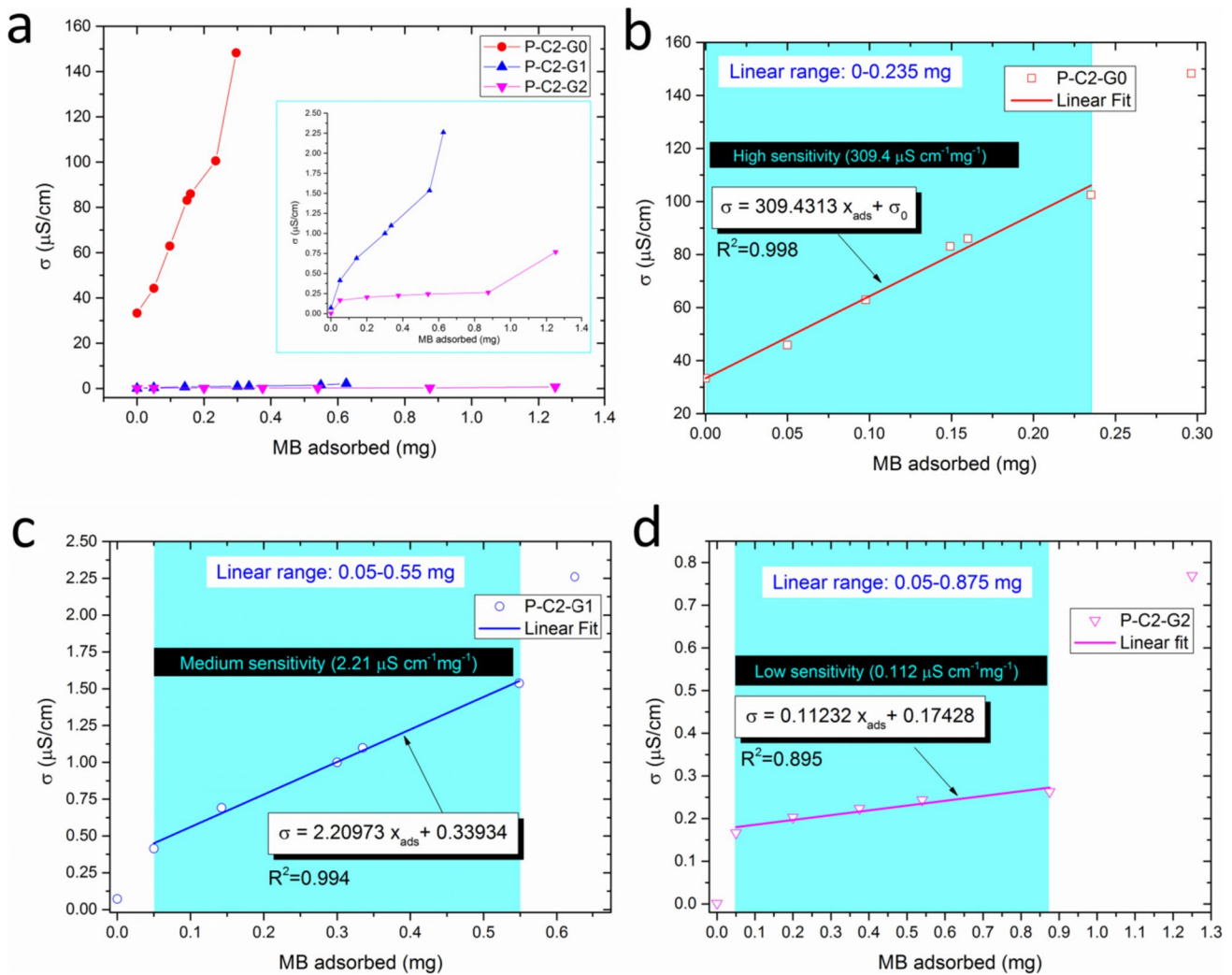
Fig. 10 Relationship between electrical conductivity and amount of MB adsorbed for nanocomposite mats (**a**); linear fit of conductivity as a function of adsorbed dye for P-C2-G0 (**b**), P-C2-G1 (**c**), and P-C2-G2 (**d**)

achieved above 70% surface coverage. Furthermore, due to the high repeatability and reliability of sorption data, precisely fitted by kinetic and isotherm models, the behavior of sorbent mats can be easily followed by monitoring the changes in electrical resistance, for instance by constructing a simple home-made device equipped with a red LED that turns on as soon as the system has adsorbed the desired amount of dye (see digital photographs in Fig. 11). These outstanding results suggest that these sorbents after usage could be eventually employed in a wealth of novel applications, including proximity sensors, piezoresistive sensors, and more generally, all the application fields in which flexible conductors are requested

[64], thus potentially transforming a waste material into a high-added value product.

Figure 12 provides the responsivity of P-C2-G0 when subjected to various standard weights. Notably, the response exhibited exceptional linearity with a sensitivity of 2 mV per gram, approximately equal to 15 mV/kPa. Furthermore, the measurements demonstrated strong reliability and repeatability. This was confirmed by the consistent return of values (6 mV and 2 mV) when applying 3 g and 1 g weights, respectively, in subsequent measurements, matching the results obtained in previous trials. These findings suggest that such materials could serve to precisely detect small values of weight or pressure.

Fig. 11 Relationship between the electrical conductivity of materials and the fraction of surface sites covered with MB molecules (q/q_m), along with the possibility to monitor the saturation state of a P-C2-G0 device by a red LED
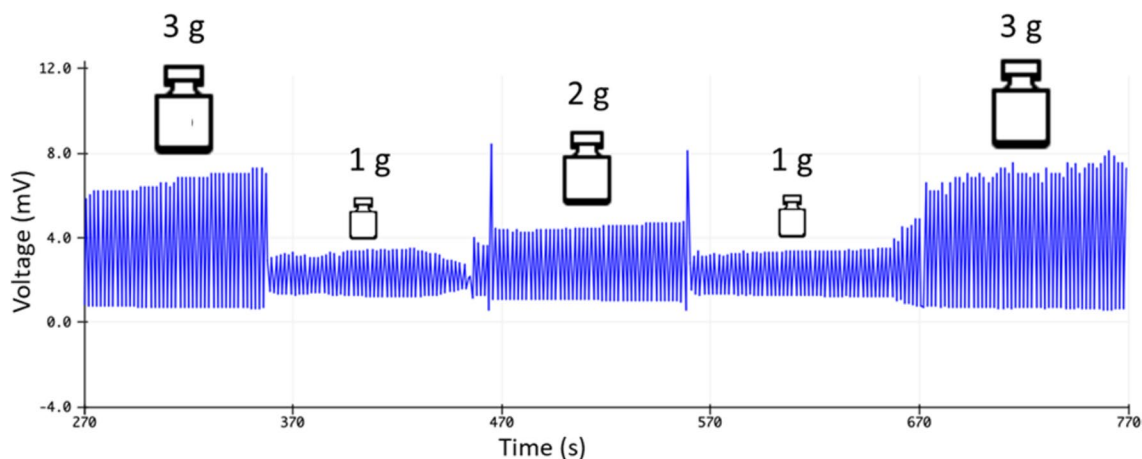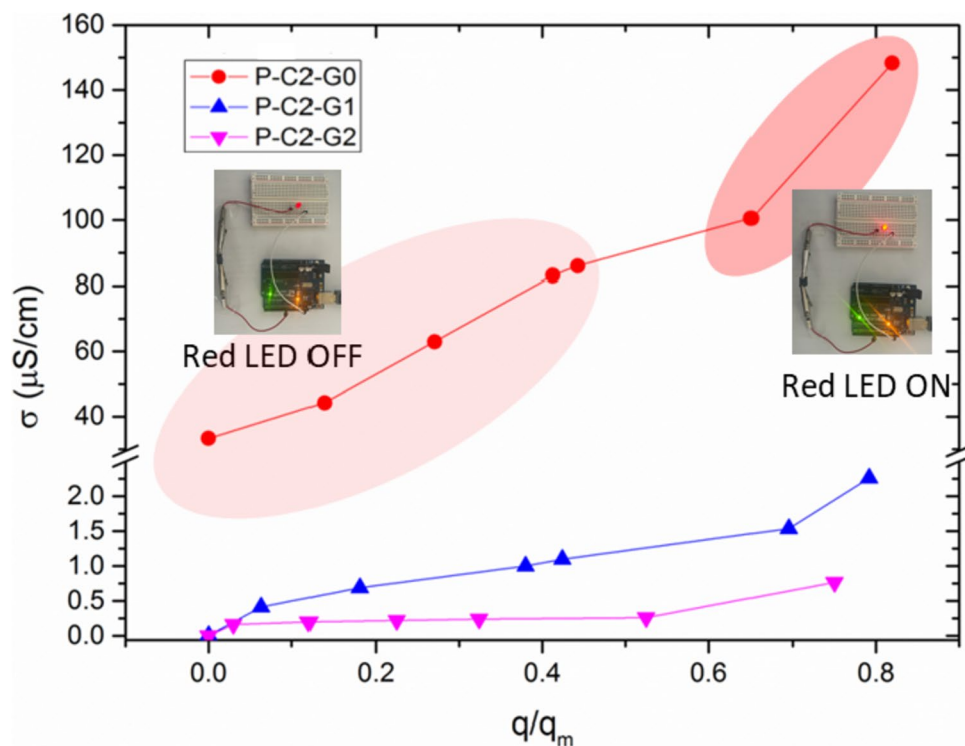

Fig. 12 Voltage–time plots reporting the responsivity of P-C2-G0 when subjected to various standard weights of 1, 2, and 3 g

4 Conclusions

We prepared PVDF-HFP-based fibrous mats containing 2% CNTs and 0%, 1%, or 2% GO by electrospinning. All the materials display randomly oriented and interconnected fibers with a bimodal size distribution. Adding nanofillers results in a progressive change of the morphology and physicochemical features of the materials. Upon increasing the filler(s) content, the progressive reduction of fiber diameter was found, with the conspicuous presence of nanoparticles emerging from the surface, whereas roughness and wettability proved

to enhance. The materials, tested as sorbents for removing MB molecules from stagnant water, displayed high values of sorption capacities that obey to the Langmuir model. The sample containing 2% CNT and 2% GO showed the highest value of 555 mg/g, while the sample containing CNTs only exhibited the lowest performance (120 mg/g). This aspect could be ascribed to the different arrangements of MB molecules onto the surface of materials, via either vertical binding or parallel stacking, depending on the prevalence of oxygen moieties or sp^2 aromatic frameworks, respectively. Nevertheless, the high values generally achieved suggest

that incorporating nanofillers activated the polymer matrix, making this latter more capable to adsorb MB dye. Kinetic studies point out that neat copolymer and hybrid materials follow a pseudo-second order adsorption mechanism, which is governed by chemisorption and intraparticle diffusion, whereas mats containing solely CNTs follow a pseudo-first order mechanism, with film diffusion as a rate-limiting step. Notably, the electrical conductivity of the mats proved to be enhanced by CNTs, whereas the presence of insulating GO (due to its extremely high oxidation degree) proved to be progressively detrimental. All the samples showed an electrical conductivity linearly increasing with the amount of MB adsorbed, until a value close to saturation content. The highest sensing performance ($309.4\ \mu S\ cm^{-1}\ mg^{-1}$) was recorded in the range 0–0.235 mg of dye for the materials containing 2% CNTs. Hybrid mats containing 2% CNTs and 2% GO displayed the lowest sensing performance ($0.112\ \mu S\ cm^{-1}\ mg^{-1}$) yet the highest sorption capacity (555 mg/g), whereas those containing 2% CNTs and 1% GO showed an intermediate behavior, thus presenting the best compromise between adsorption (263.16 mg/g) and sensing performance ($2.21\ \mu S\ cm^{-1}\ mg^{-1}$). Anyhow, as the adsorption and electrical features of such samples can be precisely fitted and predicted by the various models herein implemented, these materials could be promising for multifunctional purposes, including various types of sensors. The fascinating interactions between PVDF-HFP, CNTs, GO, and MB, in fact, could be even exploited to transform waste materials into high-added-value products.

Declarations

References

1. Scaffaro R, Gammino M, Maio A (2022) Wet electrospinning-aided self-assembly of multifunctional GO-CNT@PCL core-shell nanocomposites with spider leg bioinspired hierarchical architectures. Compos Sci Technol 221:109363. https://doi.org/10.1016/j.compscitech.2022.109363

2. Maio A, Gammino M, Fortunato Gulino E, Megna B, Fara P, Scaffaro R (2020) Rapid one-step fabrication of graphene oxide-decorated polycaprolactone three-dimensional templates for water treatment. ACS Appl Polym Mater 2:4993–5005. https://doi.org/10.1021/acsapm.0c00852

3. Liu H, Gao J, Huang W, Dai K, Zheng G, Liu C, Shen C, Yan X, Guo J, Guo Z (2016) Electrically conductive strain sensing polyurethane nanocomposites with synergistic carbon nanotubes and graphene bifillers. Nanoscale 8:12977–12989. https://doi.org/10.1039/c6nr02216b

4. Wu Z, Gao S, Chen L, Jiang D, Shao Q, Zhang B, Zhai Z, Wang C, Zhao M, Ma Y, Zhang X, Weng L, Zhang M, Guo Z (n.d.) Electrically Insulated epoxy nanocomposites reinforced with synergistic core–shell SiO2@MWCNTs and montmorillonite bifillers. Macromol Chem Phys 218:1700357. https://doi.org/10.1002/macp.201700357

5. Gong S, Cui W, Zhang Q, Cao A, Jiang L, Cheng Q (2015) Integrated ternary bioinspired nanocomposites via synergistic toughening of reduced graphene oxide and double-walled carbon nanotubes. ACS Nano 9:11568–11573. https://doi.org/10.1021/acsnano.5b05252

6. Fijalkowski K (2019) 20 - Emerging contaminants in sludge (endocrine disruptors, pesticides, and pharmaceutical residues, including illicit drugs/controlled substances, etc.), in: M.N.V. Prasad, P.J. de Campos Favas, M. Vithanage, S.V. Mohan (Eds.), Ind. Munic. Sludge, Butterworth-Heinemann, pp. 455–473. https://doi.org/10.1016/B978-0-12-815907-1.00020-9

7. Kang F, Jiang X, Wang Y, Ren J, Bin Xu B, Gao G, Huang Z, Guo Z (2023) Electron-rich biochar enhanced Z-scheme heterojunctioned bismuth tungstate/bismuth oxyiodide removing tetracycline. Inorg Chem Front 10:6045–6057. https://doi.org/10.1039/D3QI01283B

8. Zeng J, Xie W, Guo Y, Zhao T, Zhou H, Wang Q, Li H, Guo Z, Bin Xu B, Gu H (2024) Magnetic field facilitated electrocatalytic degradation of tetracycline in wastewater by magnetic porous carbonized phthalonitrile resin. Appl Catal B Environ 340:123225. https://doi.org/10.1016/j.apcatb.2023.123225

9. Wang C, Liu X, Yang T, Sridhar D, Algadi H, Bin Xu B, El-Bahy ZM, Li H, Ma Y, Li T, Guo Z (2023) An overview of metal-organic frameworks and their magnetic composites for the

removal of pollutants. Sep Purif Technol 320:124144. https://doi.org/10.1016/j.seppur.2023.124144

10. Zhang H, Wang Z, Zhao Y, Cui W, Zhang X, Wang S, Walter ED, Sassi MJ, Pearce CI, Clark SB, Rosso KM (2023) Metal ion (Cr3+, Eu3+, UO22+) adsorption on gibbsite nanoplates. Eng Sci 24:896. https://doi.org/10.30919/es896

11. Alagarsamy A, Chandrasekaran S, Manikandan A (2022) Green synthesis and characterization studies of biogenic zirconium oxide (ZrO2) nanoparticles for adsorptive removal of methylene blue dye. J Mol Struct 1247:131275. https://doi.org/10.1016/j.molstruc.2021.131275

12. Tan KB, Vakili M, Horri BA, Poh PE, Abdullah AZ, Salamatinia B (2015) Adsorption of dyes by nanomaterials: recent developments and adsorption mechanisms. Sep Purif Technol 150:229–242. https://doi.org/10.1016/j.seppur.2015.07.009

13. Yadav S, Yadav A, Bagotia N, Sharma AK, Kumar S (2022) Novel composites of Pennisetum glaucum with CNT: preparation, characterization and application for the removal of safranine O and methylene blue dyes from single and binary systems. Biomass Convers Biorefinery. https://doi.org/10.1007/s13399-021-02240-z

14. Bhat M, MR A, SV M, Das S, Roymahapatra G (2023) Photocatalytic degradation of dyes by titania/ ferric oxide/polyvinyl alcohol nanocomposites. ES Gen 2:981. https://doi.org/10.30919/esg981

15. Jasmine J, Murugan K, Ponvel AM (2023) Synthesis of Ag2CdS2/ Carbon nanocomposites for effective solar-driven dye photodegradation and electrochemical application. ES Energy Environ 20:898. https://doi.org/10.30919/esee898

16. Oladoye PO, Ajiboye TO, Omotola EO, Oyewola OJ (2022) Methylene blue dye: toxicity and potential elimination technology from wastewater. Results Eng 16:100678. https://doi.org/10.1016/j.rineng.2022.100678

17. Scaffaro R, Gammino M, Maio A (2023) Hierarchically structured hybrid membranes for continuous wastewater treatment via the integration of adsorption and membrane ultrafiltration mechanisms. Polymers (Basel) 15. https://doi.org/10.3390/polym15010156

18. Sri Abirami Saraswathi MS, Rana D, Kaleekkal NJ, Divya K, Nagendran A (2020) Investigating the efficacy of PVDF membranes customized with sulfonated graphene oxide nanosheets for enhanced permeability and antifouling. J Environ Chem Eng 8:104426. https://doi.org/10.1016/j.jece.2020.104426

19. Jang W, Yun J, Jeon K, Byun H (2015) PVdF/graphene oxide hybrid membranes via electrospinning for water treatment applications. RSC Adv 5:46711–46717. https://doi.org/10.1039/C5RA04439A

20. Sahu A, Dosi R, Kwiatkowski C, Schmal S, Poler JC (2023) Advanced polymeric nanocomposite membranes for water and wastewater treatment: a comprehensive review. Polymers (Basel) 15. https://doi.org/10.3390/polym15030540

21. Fouladivanda M, Karimi-Sabet J, Abbasi F, Moosavian MA (2021) Step-by-step improvement of mixed-matrix nanofiber membrane with functionalized graphene oxide for desalination via air-gap membrane distillation. Sep Purif Technol 256:117809. https://doi.org/10.1016/j.seppur.2020.117809

22. Cao Y, Huang J, Peng X, Cao D, Galaska A, Qiu S, Liu J, Khan MA, Young DP, Ryu JE, Feng H, Yerra N, Guo Z (2017) Poly(vinylidene fluoride) derived fluorine-doped magnetic carbon nanoadsorbents for enhanced chromium removal. Carbon NY 115:503–514. https://doi.org/10.1016/j.carbon.2017.01.033

23. Wang X, Xiao C, Liu H, Huang Q, Fu H (2018) Fabrication and properties of PVDF and PVDF-HFP microfiltration membranes. J Appl Polym Sci 135:46711. https://doi.org/10.1002/app.46711

24. Sarbatly R, Krishnaiah D, Kamin Z (2016) A review of polymer nanofibres by electrospinning and their application in oil-water separation for cleaning up marine oil spills. Mar Pollut Bull 106:8–16. https://doi.org/10.1016/j.marpolbul.2016.03.037

25. de Figueiredo Neves T, Camparotto NG, Rodrigues EA, Mastelaro VR, Dantas RF, Prediger P (2022) New graphene oxide-safranin modified@polyacrylonitrile membranes for removal of emerging contaminants: the role of chemical and morphological features. Chem Eng J 446:137176. https://doi.org/10.1016/j.cej.2022.137176

26. Maio A, Botta L, Tito AC, Pellegrino L, Daghetta M, Scaffaro R (2014) Statistical study of the influence of CNTs Purification and plasma functionalization on the properties of polycarbonate-CNTs nanocomposites. Plasma Process Polym 11:664–677. https://doi.org/10.1002/ppap.201400008

27. Scaffaro R, Maio A, Tito AC (2012) High performance PA6/ CNTs nanohybrid fibers prepared in the melt. Compos Sci Technol 72. https://doi.org/10.1016/j.compscitech.2012.08.010

28. Scaffaro R, Maio A (2019) Integrated ternary bionanocomposites with superior mechanical performance via the synergistic role of graphene and plasma treated carbon nanotubes. Compos Part B Eng. https://doi.org/10.1016/j.compositesb.2019.03.076

29. Maio A, Fucarino R, Khatibi R, Rosselli S, Bruno M, Scaffaro R (2015) A novel approach to prevent graphene oxide re-aggregation during the melt compounding with polymers. Compos Sci Technol 119:131–137. https://doi.org/10.1016/j.compscitech.2015.10.006

30. Yuan C, Su L, Yang K, Li Z, Cheng X, Wang Y, Li L (2015) Effect of pressure on the structure and properties of polymeric gel based on polymer PVdF-HFP and ionic liquid [BMIM] [BF4]. Colloid Polym Sci 293:925–932. https://doi.org/10.1007/s00396-014-3466-7

31. Simonin J-P (2016) On the comparison of pseudo-first order and pseudo-second order rate laws in the modeling of adsorption kinetics. Chem Eng J 300:254–263. https://doi.org/10.1016/j.cej.2016.04.079

32. Naseri N, Mathew AP, Oksman K (2016) Electrospinnability of bionanocomposites with high nanocrystal loadings: the effect of nanocrystal surface characteristics. Carbohydr Polym 147:464–472. https://doi.org/10.1016/j.carbpol.2016.04.018

33. Ghafari R, Scaffaro R, Maio A, Gulino EF, Lo Re G, Jonoobi M (2020) Processing-structure-property relationships of electrospun PLA-PEO membranes reinforced with enzymatic cellulose nanofibers. Polym Test 81. https://doi.org/10.1016/j.polymertesting.2019.106182

34. Naficy S, Jalili R, Aboutalebi SH, Gorkin RA III, Konstantinov K, Innis PC, Spinks GM, Poulin P, Wallace GG (2014) Graphene oxide dispersions: tuning rheology to enable fabrication. Mater Horiz 1:326–331. https://doi.org/10.1039/C3MH00144J

35. Shao J-J, Lv W, Yang Q-H (2014) Self-assembly of graphene oxide at interfaces. Adv Mater 26:5586–5612. https://doi.org/10.1002/adma.201400267

36. Kim F, Cote LJ, Huang J (2010) Graphene oxide: surface activity and two-dimensional assembly. Adv Mater 22:1954–1958. https://doi.org/10.1002/adma.200903932

37. Ruan L, Yao X, Chang Y, Zhou L, Qin G, Zhang X (2018) Properties and applications of the β phase Poly(vinylidene fluoride). Polymers (Basel) 10. https://doi.org/10.3390/polym10030228

38. Mani MR, Gebrekrstos A, Madras G, Pötschke P, Bose S (2018) PVDF–MWNT interactions control process induced β-lamellar morphology and orientation in the nanocomposites. Phys Chem Chem Phys 20:24821–24831. https://doi.org/10.1039/C8CP03739F

39. He Z, Rault F, Lewandowski M, Mohsenzadeh E, Salaün F (2021) Electrospun PVDF nanofibers for piezoelectric applications: a review of the influence of electrospinning parameters on the β phase and crystallinity enhancement. Polymers (Basel) 13. https://doi.org/10.3390/polym13020174

40. Kalimuldina G, Turdakyn N, Abay I, Medeubayev A, Nurpeissova A, Adair D, Bakenov Z (2020) A review of piezoelectric PVDF

film by electrospinning and its applications. Sensors 20. https://doi.org/10.3390/s20185214

41. Damaraju SM, Wu S, Jaffe M, Arinzeh TL (2013) Structural changes in PVDF fibers due to electrospinning and its effect on biological function. Biomed Mater 8:45007. https://doi.org/10.1088/1748-6041/8/4/045007

42. Scaffaro R, Maio A, Lo Re G, Parisi A, Busacca A (2018) Advanced piezoresistive sensor achieved by amphiphilic nanointerfaces of graphene oxide and biodegradable polymer blends. Compos Sci Technol 156. https://doi.org/10.1016/j.compscitech.2018.01.008

43. Scaffaro R, Maio A, Lopresti F, Botta L (2017) Nanocarbons in electrospun polymeric nanomats for tissue engineering: a review. Polymers (Basel) 9. https://doi.org/10.3390/polym9020076

44. Maio A, Pibiri I, Morreale M, La Mantia FP, Scaffaro R (2021) An overview of functionalized graphene nanomaterials for advanced applications. Nanomaterials 11. https://doi.org/10.3390/nano11071717

45. Elmaghraby NA, Omer AM, Kenawy E-R, Gaber M, Hassaan MA, Ragab S, Hossain I, El Nemr A (2023) Electrospun cellulose acetate/activated carbon composite modified by EDTA (rC/AC-EDTA) for efficient methylene blue dye removal. Sci Rep 13:9919. https://doi.org/10.1038/s41598-023-36994-5

46. Hussain Z, Ullah S, Yan J, Wang Z, Ullah I, Ahmad Z, Zhang Y, Cao Y, Wang L, Mansoorianfar M, Pei R (2022) Electrospun tannin-rich nanofibrous solid-state membrane for wastewater environmental monitoring and remediation. Chemosphere 307:135810. https://doi.org/10.1016/j.chemosphere.2022.135810

47. Ali ASM, El-Aassar MR, Hashem FS, Moussa NA (2019) Surface modified of cellulose acetate electrospun nanofibers by polyaniline/β-cyclodextrin composite for removal of cationic dye from aqueous medium. Fibers Polym 20:2057–2069. https://doi.org/10.1007/s12221-019-9162-y

48. Sundaran SP, Reshmi CR, Sagitha P, Manaf O, Sujith A (2019) Multifunctional graphene oxide loaded nanofibrous membrane for removal of dyes and coliform from water. J Environ Manage 240:494–503. https://doi.org/10.1016/j.jenvman.2019.03.105

49. Pervez MN, Talukder ME, Mishu MR, Buonerba A, Del Gaudio P, Stylios GK, Hasan SW, Zhao Y, Cai Y, Figoli A, Zarra T, Belgiorno V, Song H, Naddeo V (2022) One-step fabrication of novel polyethersulfone-based composite electrospun nanofiber membranes for food industry wastewater treatment. Membranes (Basel) 12. https://doi.org/10.3390/membranes12040413

50. Beiranvand R, Sarlak N (2023) Electrospun nanofiber mat of graphene/mesoporous silica composite for wastewater treatment. Mater Chem Phys 309:128311. https://doi.org/10.1016/j.matchemphys.2023.128311

51. Zhao R, Wang Y, Li X, Sun B, Jiang Z, Wang C (2015) Water-insoluble sericin/β-cyclodextrin/PVA composite electrospun nanofibers as effective adsorbents towards methylene blue. Colloids Surf B Biointerfaces 136:375–382. https://doi.org/10.1016/j.colsurfb.2015.09.038

52. Ma F, Zhang D, Huang T, Zhang N, Wang Y (2019) Ultrasonication-assisted deposition of graphene oxide on electrospun poly(vinylidene fluoride) membrane and the adsorption behavior. Chem Eng J 358:1065–1073. https://doi.org/10.1016/j.cej.2018.10.121

53. W. Chen, H. Ma, B. Xing, Electrospinning of multifunctional cellulose acetate membrane and its adsorption properties for ionic

dyes. Int J Biol Macromol 158:1342–1351. https://doi.org/10.1016/j.ijbiomac.2020.04.249

54. Xing R, Wang W, Jiao T, Ma K, Zhang Q, Hong W, Qiu H, Zhou J, Zhang L, Peng Q (2017) Bioinspired polydopamine sheathed nanofibers containing carboxylate graphene oxide nanosheet for high-efficient dyes scavenger. ACS Sustain Chem Eng 5:4948–4956. https://doi.org/10.1021/acssuschemeng.7b00343

55. de Farias LMS, Ghislandi MG, de Aguiar MF, Silva DBRS, Leal ANR, de A.O. Silva F, Fraga TJM, de Melo CP, Alves KGB (2022) Electrospun polystyrene/graphene oxide fibers applied to the remediation of dye wastewater. Mater Chem Phys 276:125356. https://doi.org/10.1016/j.matchemphys.2021.125356

56. Pathirana MA, Dissanayake NSL, Wanasekara ND, Mahltig B, Nandasiri GK (2023) Chitosan-graphene oxide dip-coated polyacrylonitrile-ethylenediamine electrospun nanofiber membrane for removal of the dye stuffs methylene blue and Congo red. Nanomaterials 13. https://doi.org/10.3390/nano13030498

57. Mohammad N, Atassi Y (2020) Adsorption of methylene blue onto electrospun nanofibrous membranes of polylactic acid and polyacrylonitrile coated with chloride doped polyaniline. Sci Rep 10:13412. https://doi.org/10.1038/s41598-020-69825-y

58. Bangari RS, Yadav A, Bharadwaj J, Sinha N (2022) Boron nitride nanosheets incorporated polyvinylidene fluoride mixed matrix membranes for removal of methylene blue from aqueous stream. J Environ Chem Eng 10:107052. https://doi.org/10.1016/j.jece.2021.107052

59. Arias Arias F, Guevara M, Tene T, Angamarca P, Molina R, Valarezo A, Salguero O, Vacacela Gomez C, Arias M, Caputi LS (2020) The adsorption of methylene blue on eco-friendly reduced graphene oxide. Nanomaterials 10. https://doi.org/10.3390/nano10040681

60. Wu F-C, Tseng R-L, Juang R-S (2009) Initial behavior of intraparticle diffusion model used in the description of adsorption kinetics. Chem Eng J 153:1–8. https://doi.org/10.1016/j.cej.2009.04.042

61. Schwaab M, Steffani E, Barbosa-Coutinho E, Severo Júnior JB (2017) Critical analysis of adsorption/diffusion modelling as a function of time square root. Chem Eng Sci 173:179–186. https://doi.org/10.1016/j.ces.2017.07.037

62. Wojtoniszak M, Rogińska D, Machaliński B, Drozdzik M, Mijowska E (2013) Graphene oxide functionalized with methylene blue and its performance in singlet oxygen generation. Mater Res Bull 48:2636–2639. https://doi.org/10.1016/j.materresbull.2013.03.040

63. Ocak YS, Kulakci M, Kılıçoğlu T, Turan R, Akkılıç K (2009) Current–voltage and capacitance–voltage characteristics of a Sn/Methylene Blue/p-Si Schottky diode. Synth Met 159:1603–1607. https://doi.org/10.1016/j.synthmet.2009.04.024

64. Li T, Wei H, Zhang Y, Wan T, Cui D, Zhao S, Zhang T, Ji Y, Algadi H, Guo Z, Chu L, Cheng B (2023) Sodium alginate reinforced polyacrylamide/xanthan gum double network ionic hydrogels for stress sensing and self-powered wearable device applications. Carbohydr Polym 309:120678. https://doi.org/10.1016/j.carbpol.2023.120678

Publisher's Note Springer Nature remains neutral with regard to jurisdictional claims in published maps and institutional affiliations.